Stationary Atmospheric Responses to an Idealized Sea Surface Temperature Anomaly in the Southern Ocean.

Guillaume Maze, Fabio d'Andrea, Alain Colin de Verdiere, Patrice Klein

Stationary Atmospheric Responses to an Idealized Sea Surface Temperature Anomaly in the Southern Ocean

Guillaume Maze

Laboratoire de Physique des Océans, UMR 6523, Ifremer, CNRS, IRD, UBO, Plouzané, France

Fabio D'Andrea

Laboratoire de Météorologie Dynamique, École Normale Supérieure, Paris, France

Alain Colin de Verdière and Patrice Klein

Laboratoire de Physique des Océans, Brest, France

ABSTRACT

The stationary atmospheric response to an idealized sea surface temperature anomaly (SSTA) is studied with a quasigeostrophic atmospheric model of the Southern Hemisphere. Sensitivity of the stationary response to the midlatitude SSTA location is determined and responses are decomposed on vertical modes.

The SSTA almost directly forces baroclinic responses, inducing warm-air anomalies 40°–50° downstream, eastward, to the SSTA. These baroclinic responses arise from an equilibrium between the SSTA-induced anomalous vortex stretching and (i) advection by the quasi-stationary flow and (ii) dissipation by high-frequency eddies.

The barotropic response consists of a midlatitude ridge (trough) and a South Pole trough (ridge) for SSTAs localized from the Drake Passage to the western Indian Ocean (from south of Australia to the center of the Pacific Ocean). This response can be further decomposed into (i) a zonally asymmetric component, a quasi-stationary wave train forced by a barotropic ridge downstream of the SSTA; and (ii) a zonal-mean component similar to a meridional shift of westerlies and hence a southern annular mode (SAM)-like pattern. The former component is phase locked with the SSTA position, while the latter has a phase that depends on the relative SSTA position with regard to the background quasi-stationary wave pattern. The study shows that the barotropic downstream ridge response is responsible for modifying the low-frequency eddy–mean flow interactions through relative vorticity fluxes and inducing the bipolar projection of the zonal-mean response.

1. Introduction

The Southern Hemisphere midlatitudes are characterized by strong zonal jets in the atmosphere and a strong zonal current in the ocean, the Antarctic Circumpolar Current (ACC). The principal mode of atmospheric variability is the hemispheric seesaw described under different names, such as "zonal wind vacillation" and "high-latitude mode" (Kidson 1988; Hartmann and Lo 1998). Following Thompson and Wallace (2000), we will refer to this mode as the southern annular mode (SAM). The SAM has been shown to dominate the large-scale

Southern Hemisphere–coupled variability (Hall and Visbeck 2002; Simmonds 2003; Codron 2007).

Other studies (e.g., White 2004 and references therein) tend to attribute more importance to a coupled mode of variability called Antarctic circumpolar wave. This mode would explain the fact that sea surface temperatures (SST) anomalies were observed to propagate eastward along the ACC from the mid-1980s to the mid-1990s (Connolley 2002). Works by Maze et al. (2006, hereafter M06) and Verdy et al. (2006) show how the eastward propagation can be largely explained as a passive transport of SST anomalies by the ACC, where the SST anomalies are generated by the SAM through Ekman surface heat flux or through remote forcing by El Niño–Southern Oscillation (ENSO). An oceanic feedback on the atmospheric forcing is present though weak and is

Corresponding author address: Guillaume Maze, Laboratoire de Physique des Océans, IFREMER, BP 70, 29280 Plouzané, France.
E-mail: gmaze@ifremer.fr

likely to increase the lifespan of SST anomalies (M06; Watterson 2000, 2001). The importance of this feedback depends crucially on the atmospheric response to the SST anomaly (SSTA).

During the second half of the twentieth century, positive trends in geopotential height anomalies over the South Pole and at midlatitudes were observed (Thompson and Solomon 2002). These trends project positively on the SAM pattern (Thompson and Wallace 1998). An extensive list of literature has been produced to explain this trend, and two causes of anthropogenic origin are clearly identified (i) ozone depletion in the polar stratosphere—reducing shortwave radiation absorption, cooling the polar air, and through multiple dynamical responses inducing a positive shift in the SAM (e.g., Gillett and Thompson 2003; Perlwitz et al. 2008); and (ii) warming in the global tropical oceans (e.g., Grassi et al. 2005). Unlike the ozone depletion mechanism, the role of tropical ocean's warming on the SAM trend is still being debated among scientists though, simply because the Southern Hemisphere atmospheric response to ocean's warming can show different and contradictory patterns [see Li et al. (2010) and references therein].

Interactions between sea surface temperatures anomalies (in the tropics and extratropics) and the atmospheric circulation in midlatitudes have long been studied (e.g., Smagorinsky 1953). But the response of the atmosphere in midlatitudes is—in general—small in comparison to its internal variability, which makes it very difficult to measure. Moreover, many experiments have been conducted making use of general circulation models—both in a coupled or in a forced configuration—and large differences in behavior have been found depending on the region, the season, and the model used [see Kushnir et al. (2002); Li et al. (2010) and references therein]. When a dynamical balance is established between eddy forcing and linear advection, the atmospheric response can resemble the large-scale modes of unforced atmospheric variability (Peng and Robinson 2001; Son and Lee 2005; Watterson 2010). However, given different large-scale basic states, different responses are possible in terms of linear response to heating (Hall et al. 2001). According to the basic state, the nonlinear effect of the transient baroclinic eddy forcing can also become more or less important and characterized by different time scales of action (Peng and Whitaker 1999; Inatsu et al. 2003; Kravtsov et al. 2009).

For all the uncertainties listed above, we propose in this study to determine the atmospheric response to an idealized SST anomaly in the Southern Ocean. The strategy is to focus on the stationary response sensitivity to a midlatitude SSTA forcing position to answer the following questions: (i) what is the potential impact of an

SSTA transported by the ACC on the overlying atmosphere and (ii) is the SAM sensitive to midlatitude SSTAs? In section 2 the model setup is described in detail, along with a description of the experiments conducted. In section 3 the atmospheric responses are described, and in section 4 their dynamical balance is explained. Results are discussed in section 5, and we conclude in section 6.

2. Model and experiments

a. Model description

The atmospheric model (see Fig. 1) is quasigeostrophic (QG) with the global domain on the sphere and pressure as a vertical coordinate; it was developed by Marshall and Molteni (1993). A version of this model, coupled to a slab mixed ocean layer, was used by D'Andrea et al. (2005) and M06 for studies of the North Atlantic and the Southern Ocean climate variability. The conservation equation of the quasigeostrophic potential vorticity (PV)

$$\frac{\partial q}{\partial t} = -J(\psi, q) - \frac{f_0 R}{C_{pa}} \frac{\partial}{\partial p}\left(\frac{Q}{p\sigma}\right) - D(\psi) + S \quad \text{with}$$

(1)

$$q = \nabla^2 \psi + f + f_0^2 \frac{\partial}{\partial p}\left(\frac{1}{\sigma}\frac{\partial \psi}{\partial p}\right)$$

(2)

is solved on the sphere with a T21 horizontal resolution (triangular truncation) at the pressure levels 200, 500, and 800 hPa and integrated in time with a predictor–corrector scheme (first-order Adams–Bashforth–Mouton) with a time step of 1 h. The discretized PV prognostic equations are

$$\frac{Dq_1}{Dt} = -D_1 + S_1,$$

(3)

$$\frac{Dq_2}{Dt} = -D_2 - \frac{Q_{650}(\psi_{2,3}, T)}{K_b R_b^2 C_{pa}} + S_2, \quad \text{and}$$

(4)

$$\frac{Dq_3}{Dt} = -D_3 + \frac{Q_{650}(\psi_{2,3}, T)}{K_b R_b^2 C_{pa}} + S_3,$$

(5)

where $D \cdot /Dt = \partial_t \cdot + J(\psi_i, \cdot)$ is the total derivation operator, including PV advection by the QG streamfunctions ψ_i; and D_i represent linear dissipation terms, including Ekman dissipation (orography dependent) and Newtonian thermal relaxation between the layers. Orographic effects are included in the PV definition at the lower level 3 (800 hPa).

Recent studies have shown that sea surface temperature fronts can influence the atmosphere up to the
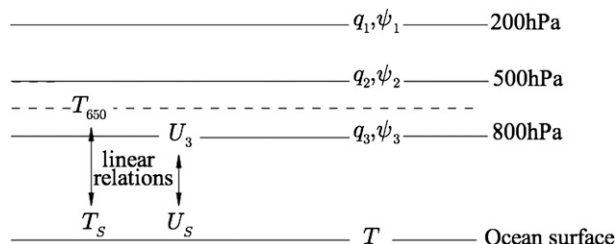
FIG. 1. Schematic of the vertical discretization of the model.

tropopause level through vertical penetration of anomalous air–sea fluxes (Minobe et al. 2008). However, given the QG hypothesis, we do not expect this frontal process to occur in our model. Following previous studies (e.g., Peng and Whitaker 1999; Ferreira and Frankignoul 2005, 2008; M06), we will assume the penetration of the air–sea surface diabatic forcing to be contained in the lower atmosphere, that is, to be no higher than 500 hPa. In the lower layer, the diabatic heat source is computed as $Q_{650} = (g/\Delta p)F$, where $g/\Delta p$ ($\Delta p = 420$ mb) is a measure of the lower-layer thickness and F represents air–sea turbulent (sensible and latent) heat fluxes. The second term on the rhs of (4) and (5) is thus the PV tendency due to heat exchanges with the ocean. It depends on Q_{650} and C_{pa} (the specific heat at constant volume for dry air); $K_b = f_0 p_b/(R\delta p)$ is the coefficient linking streamfunctions at 500 and 800 hPa to the temperature at 650 hPa through the thermal wind balance; and $R_b = 450$ km is the Rossby radius of the lower layer [these coefficients appear when the second rhs term of (1) is discretized]. The air–sea turbulent heat flux F is given by the following bulk aerodynamic formula:

$$F(\psi_{2,3}, T) = \rho_a C_D C_{pa}(1 + B^{-1})|\mathbf{U}_s|(\text{SST} - T_s), \qquad (6)$$

where ρ_a is the dry air density; $C_D = 1.3 \times 10^{-3}$ is a constant drag coefficient; $B = 0.5$ is the Bowen factor (ratio between sensible and latent heat fluxes); $|\mathbf{U}_s|$ is the surface wind intensity; SST is the sea surface temperature; and T_s is the surface atmospheric temperature. Surface atmospheric variables are taken at 10-m height.

We introduced in the PV equations a time-independent source term S_i that represents all adiabatic and subgrid processes (D'Andrea and Vautard 2000) to give the model a realistic wintertime climatology. Winter was chosen as the season when coupling is strongest between the atmosphere and the ocean. The forcing term S_i is computed empirically as the mean residual of (3)–(5) with respect to observations following the method introduced by Roads (1987). The data used as "observations" were a twice-daily European Centre for Medium-Range Weather Forecasts (ECMWF) analysis dataset ranging

from June 1979 to August 1993 [15-year ECMWF Re-Analysis (ERA-15); Gibson et al. 1996; June–August (JJA)] and SST from Reynolds and Smith (1994). In the case of the Southern Hemisphere, this method gave a considerable high pressure error over the Antarctic continent. Consequently, we added a zonal-mean temperature correction to all S_i (see appendix A for more details).

Because the atmospheric heat source Q_{650} is not directly prescribed but depends on the SST through air–sea heat fluxes [see (6)], sea surface atmospheric variables need to be diagnosed. The method used is a local linear relation between variables of the atmospheric lower layer and the sea surface. Local wind components are linearly computed from those at 800 hPa (diagnosed from ψ_3 obtained by inversion of q_3). Local sea surface atmospheric temperature T_s is linearly computed from the temperature at 650 hPa diagnosed using the thermal wind balance between the 500- and 800-hPa levels. The same dataset used to compute forcing terms S_i (see above) is analyzed to derive local coefficients of these linear relations. Surface wind amplitude is found to be approximately half the wind at 800 hPa, and surface temperature is 1.2 times the one at 650 hPa.

b. Description of the experiments

We carried out 14 experiments, all of them under perpetual JJA conditions, with idealized SSTAs centered at 47°S and 14 longitudes equally spaced along a latitude circle, starting from the Greenwich meridian (see Fig. 2a).

As a reference for these experiments, a control run is performed with the climatological SST field from a fully coupled version of the model that was studied by M06 [we checked to see that using this SST field instead of the observation dataset Reynolds and Smith (1994) used to compute S_i terms does not induce significant source/sink of PV]. The stationary atmospheric response to one of the SST anomalies is defined as the long-term mean difference between the simulation with the SSTA and the control one.

The idealized SSTA used in the present study has a 2D Gaussian shape. It has been fitted on the mean composite SSTA found by M06 (see their Fig. 6), and it synthesizes the aspect of a typical SSTA in midlatitudes of the Southern Ocean. The SST anomaly has a spatial scale of 80° in the zonal direction and 10° in the meridional one, that is, 6000 km × 1200 km at midlatitudes (see Fig. 2b).

Many studies force an atmospheric model with an SSTA of a few degrees of amplitude to enhance the response by increasing the signal-to-noise ratio (Kushnir et al. 2002). However, a major drawback of this method

(A) All 14 SSTa center locations

(B) One SSTa pattern example (Exp. 1 in A)

(C) Barotropic quasi−stationary wave from Control run Z
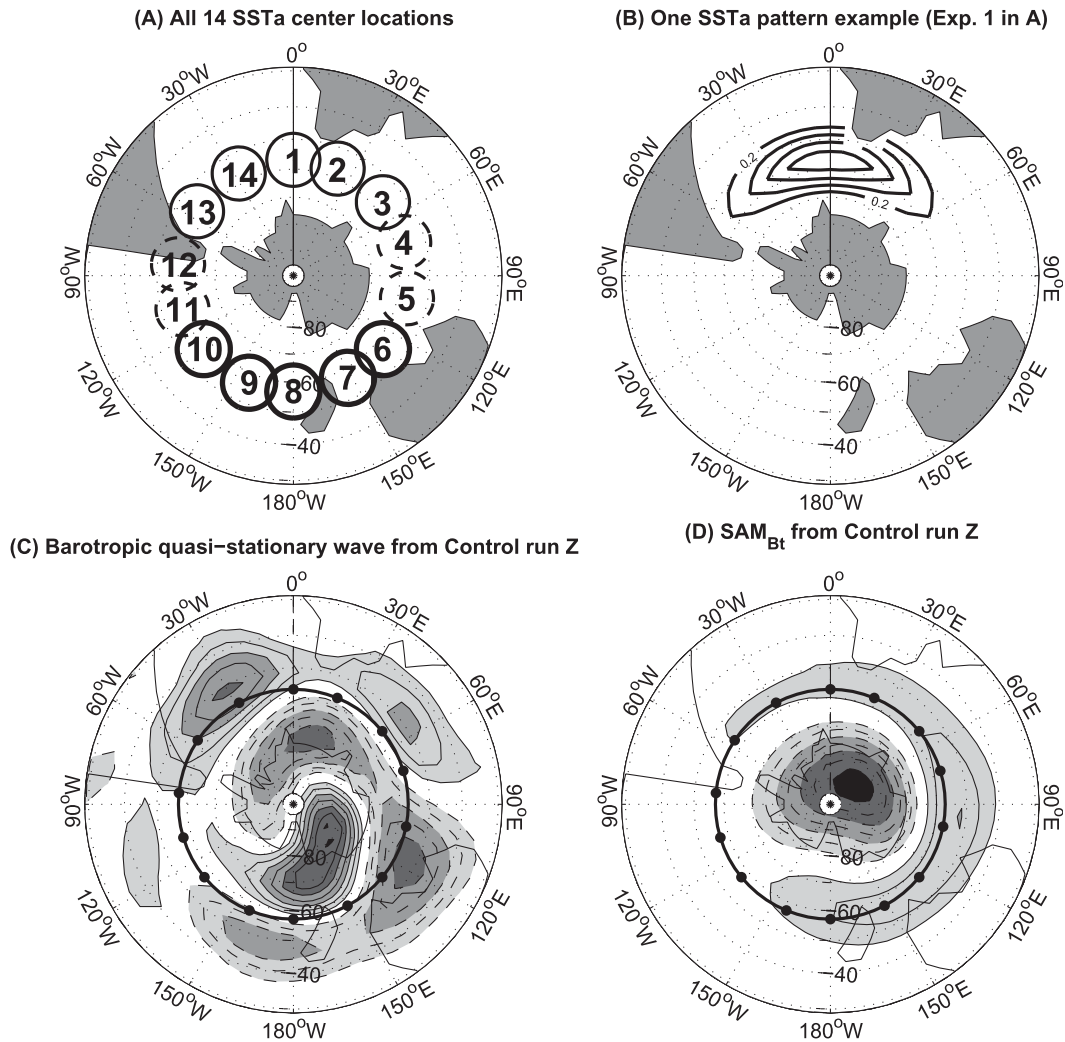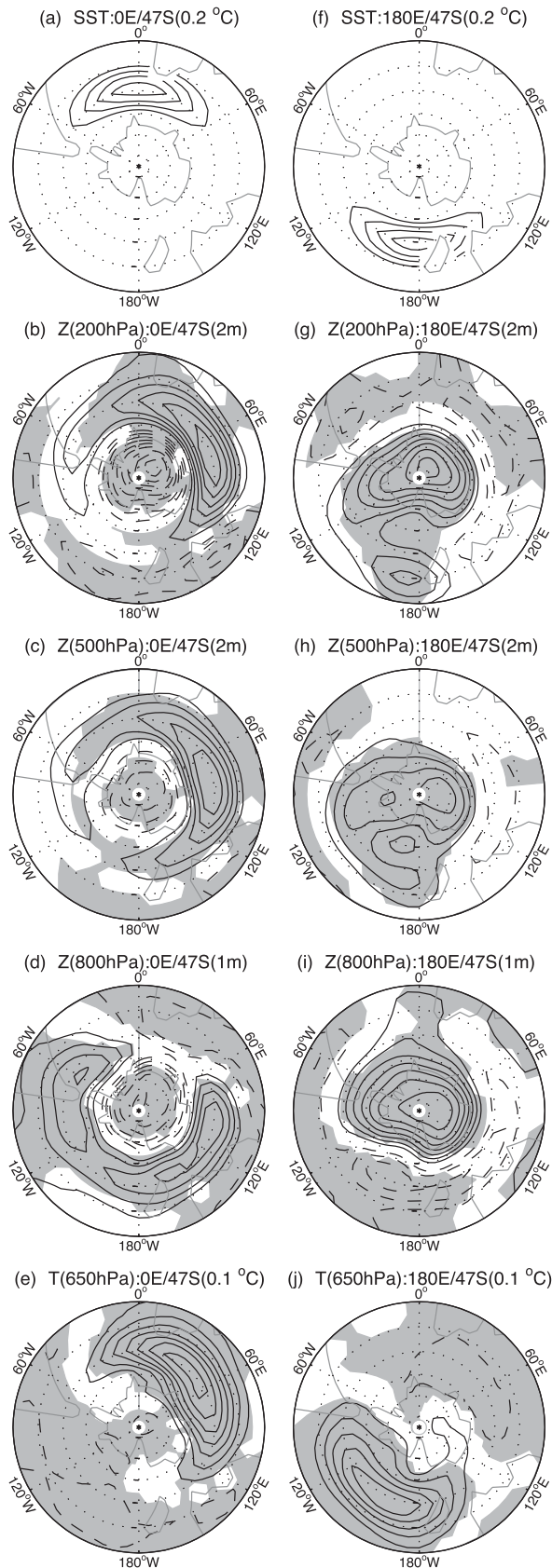
(D) SAM$_{Bt}$ from Control run Z

FIG. 2. (a) Locations of the SSTA center for the 14 experiments. Light or heavy solid circles are for barotropic responses projecting on a positive or a negative SAM phase, and light dashed circles are for intermediate cases; see text for more details. (b) SSTA pattern centered at 0° with a 1°C amplitude. Contours every 0.2°C. (c) Quasi-stationary wave of the control simulation from the geopotential height barotropic component (departure from the zonal mean of the time-mean 7-day low-pass-filtered field). Contours every 20 m, negative dashed, and zero contour omitted. (d) Barotropic component of the SAM for the control simulation (contours every 20 m, negative contours are dashed, and the zero contour omitted). SAM is defined as the first principal component of the monthly geo-potential height anomalies. Shading in (c),(d) is based on magnitude, and the heavy black line recalls the latitude circle (47°S) of all SSTAs, which is also indicated by the dots.

is that it requires a linear downscaling of the response amplitude to be expressed for a SSTA of 1°C to compare results from one study to another. Because of the low numerical cost of the model used in the present study, we can afford to avoid this method. Having fixed the SSTA to a realistic, although still large, amplitude of 1°C, we estimated that an integration length of 50 years was necessary to obtained large statistically significant centers of action in the response patterns. This time scale makes our responses eventually valid for climatic trends, as those discussed in the introduction. Note that

to analyze simple maps without the need to overlay significant pattern regions, the integrations performed were of 200—perpetual winter—years. We will keep in mind that patterns are statistically robust over most of the domain presented.

The control run climatology has been verified to reproduce key features of the Southern Hemisphere circulation reasonably. For example, the latitude of maximum zonal winds (about 23 m s^{-1}) is ~40°S at 500 hPa, which compares well with observational es-timates [see Fig. 1 in Hartmann and Lo (1998), for

(a) SST:0E/47S(0.2 °C)   (f) SST:180E/47S(0.2 °C)

(b) Z(200hPa):0E/47S(2m)   (g) Z(200hPa):180E/47S(2m)

(c) Z(500hPa):0E/47S(2m)   (h) Z(500hPa):180E/47S(2m)

(d) Z(800hPa):0E/47S(1m)   (i) Z(800hPa):180E/47S(1m)

(e) T(650hPa):0E/47S(0.1 °C)   (j) T(650hPa):180E/47S(0.1 °C)

instance]. More details about the control simulation climatology can be found in Maze (2006). Here we present two fields relevant to our study. Figures 2c,d show the barotropic components of the quasi-stationary waves and the SAM—defined as the first EOF of the geopotential height anomalies. At midlatitudes the quasi-stationary wave pattern shows two high pressure systems in the Atlantic and Indian regions and two low pressure systems south of Australia and in the western Pacific regions. They spiral southwestward to over Antarctica. The SAM exhibits a maximum at midlatitudes southwest of Australia and a minimum in the Indian sector of Antarctica. Both fields are realistic and will be discussed in the following sections.

3. Description of stationary atmospheric responses to SSTA

a. Responses at pressure levels

SST anomalies induce anomalous air–sea heat fluxes. These in turn force anomalous heat sources in the lower layer of the atmosphere. Air–sea heat flux anomalies have a pattern very similar to the SSTA itself (not shown). The 14 experiments' ensemble mean amplitude of F stationary responses is 21.0 W m^{-2}. They vary from 26.5 W m^{-2} for the experiment with the SSTA centered at 51°E to 13.3 W m^{-2} for experiment with the SSTA centered at 180°. These amplitudes correspond to heating rates at 650 mb of 0.4, 0.5, and 0.2 K day^{-1}—values pretty much in line with standard forcing. [Butler et al. (2010) used values of 0.5 K day^{-1} to study atmospheric responses to climatic change–induced heat anomalies.] For other atmospheric variables, we also found larger response amplitudes for SSTA centered in the Atlantic/ western Indian sector and smaller response amplitudes for SSTA centered in the western Pacific.

Analysis of patterns and amplitudes from the 14 experiments has shown that responses may be grouped into two sets, each well represented by results from experiments where SSTAs are centered at 0° and 180°, shown in Figs. 3a–f. These two key experiments among

←

Fig. 3. Stationary atmospheric responses to an idealized SSTA of (a),(f) 1-K amplitude centered at 47°S and (left) 0° and (right) 180°. Geopotential height responses at (b),(g) 200, (c),(h) 500, and (d),(i) 800 hPa. (e),(j) Responses of atmospheric temperature at 650 hPa. Zero contours omitted on all plots; contours interval is indicated in parenthesis in the panels' subtitles. Gray-shaded areas indicate the 95% significance level [not shown on SSTA (a) and (f)].

the 14 we conducted will be referred to as SSTA-0 and SSTA-180, respectively, in the study.

Stationary atmospheric responses in geopotential height at 200, 500, and 800 hPa and temperature at 650 hPa are shown in Fig. 3, and left and right columns for experiments SSTA-0 and SSTA-180, respectively. Note that to plot the geopotential height response, we inverted the quasigeostrophic PV in (2) to get the geostrophic streamfunction and then computed the geopotential through

$$\nabla^2 Z = \frac{1}{g} \nabla f \nabla \psi. \tag{7}$$

Figure 3 shows the geopotential height response in the vicinity of the SSTA (represented in Figs. 3a–f) to ∼60° eastward being positive in the upper troposphere at 200 and 500 hPa, and negative at the lower level of 800 hPa. In this region close to the SSTA, the response amplitude is quite similar in all experiments: on average about −3 m at 800 hPa and 10/12 m at 500 hPa. Previous numerical studies (Frankignoul 1985; Kushnir et al. 2002) and observations (Rodwell and Folland 2002; Czaja and Frankignoul 2002) show a wide range of atmospheric response amplitude: from 10 to 40 m K^{-1} at 500 hPa. Even if our results are clearly in the lower part of this range, one should notice that these amplitudes had all been determined in the Northern Hemisphere and that a direct quantitative comparison needs to be conducted carefully.

Local atmospheric responses, in the vicinity of the SSTA direct forcing, show no fundamental differences among the 14 experiments. This response is baroclinic, a feature clearly seen in the temperature anomaly at 650 hPa (Figs. 3e–j). Pressure anomalies positive at 500 hPa and negative at 800 hPa dilate the lower layer and induce a warm temperature anomaly of 0.7°C eastward of the SSTA. Figures 3e–j show a very similar pattern between the experiments SSTA-0 and SSTA-180, again representative of all the other 12 locations of SSTA forcing.

The very large-scale structure of atmospheric responses is, in turn, different and is separate from the two sets of experiments introduced earlier in the section. On one hand, the experiment SSTA-0 shows far from the direct SSTA forcing region, geopotential height anomalies positive at midlatitudes and negative over the South Pole—an equivalent barotropic pattern that thus extends from 200 to 800 hPa. On the other hand, experiment SSTA-180 shows geopotential height anomalies of opposite sign compared to the SSTA-0 case, albeit enhanced over the South Pole and weakened at midlatitudes. These two large-scale patterns are relevant for the rest of the experiments. Features from the SSTA-0 case are similar for all the other experiments located

clockwise from the Drake Passage to the western Indian Ocean (experiments denoted as light black circles in Fig. 2a), whereas the SSTA-180 case is relevant for experiments with SSTa located between south of Australia and the center of the Pacific Ocean (heavy black circles in Fig. 2a). Outside these broad regions (light black dashed circles in Fig. 2a), weak responses exhibit intermediate patterns between the two extreme phases of the SSTA-0 and SSTA-180 experiments that we do not discuss here.

b. Vertical structure of responses

The visual inspection of all atmospheric responses suggests the superposition of an equivalent-barotropic large-scale response onto a local baroclinic one, the former being dependent on the SSTA location, while the latter is not. These different behaviors of the atmospheric response with respect to its apparent vertical structure lead us to project responses onto vertical modes. This greatly simplifies the interpretation of the results.

The three pressure levels of the model can be projected onto one barotropic and two baroclinic modes (see appendix B for more details). The barotropic mode of the response is proportional to the vertical mean; the first baroclinic mode is related to temperature anomalies having the same sign throughout the depth of the atmospheric column, whereas the second baroclinic mode is related to temperature anomalies of opposite signs in the lower and upper layers.[1] Also note that the different Rossby radius of deformation of the upper and lower layers implies that the first (second) baroclinic mode is mainly related to the upper-layer (lower layer) temperature. Figures 4–6 show the detailed geopotential height responses of Fig. 3 when projected onto the three vertical modes.

The first baroclinic mode responses are similar for all 14 experiments in the midlatitude band. Figures 4a,b show a negative geopotential height anomaly eastward of the SSTA, of about −8- and −5-m amplitude. The first baroclinic mode responses are maximum in amplitude for the SSTA located from the Atlantic Ocean to the east Indian Ocean (−14 m for experiment with the SSTA centered at 30°W) and minimum for the SSTA located in the western Pacific (about −4 m). This negative first baroclinic mode response is the sign of a stationary positive temperature anomaly throughout the depth of the atmospheric column just downstream of the

---

[1] Given that in this QG layer model, a temperature anomaly into a particular layer is related, via the thermal wind balance, to opposite geopotential height anomalies at the two pressure levels embedding the layer.
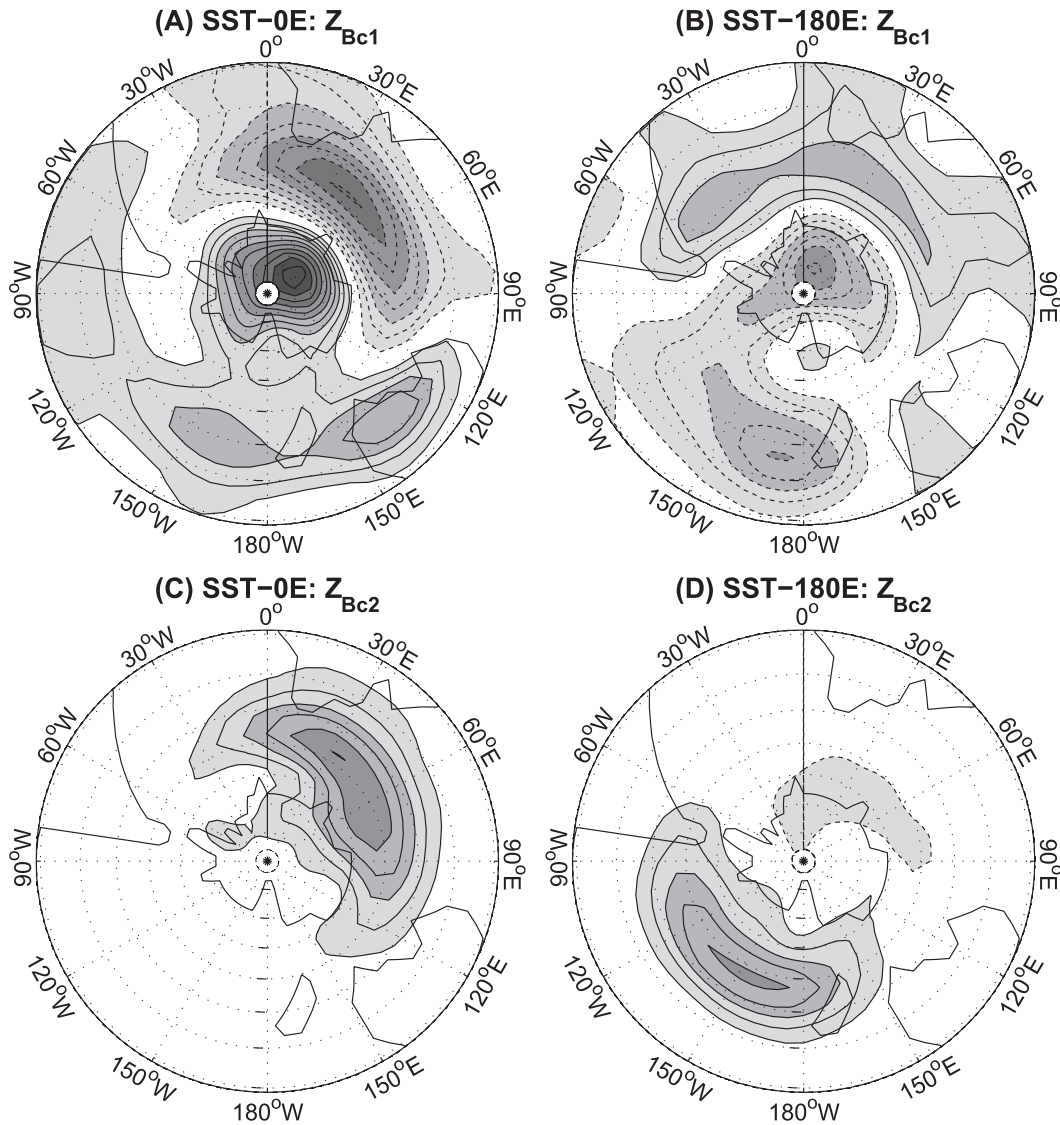
FIG. 4. Stationary atmospheric responses of geopotential height for (left) SSTA-0 and (right) SSTA-180 experiments projected on the (top) first and (bottom) second baroclinic vertical modes. Contours are every meter, negative contours are dashed, and the zero contour is omitted. Shading is based on magnitude.

SSTA [see (B5)]. Note that this warm temperature response is associated with, symmetrically to the South Pole, a cold one (positive geopotential height response)—albeit of a smaller amplitude. Over the South Pole, however, the baroclinic mode responses differ among the 14 experiments. Positive (negative) geopotential height anomalies, a cooling (warming) of the atmospheric air column, are found over the South Pole for experiments with the SSTA located between the Drake Passage and the western Indian Ocean (from south of Australia to the center of the Pacific Ocean).

The second baroclinic mode responses for all 14 experiments, shown in Figs. 4c,d, are restricted to midlatitudes

and are similar in shape. It is a positive geopotential height anomaly of 6-m amplitude, centered at midlatitudes 30° downstream of the SSTA center with an identical spatial pattern. This component of the atmospheric column response is primarily driven by a warming of the lower layer (Figs. 3e–j). Given the vertical profile of heat flux forcing induced by the SSTA [restricted to the lower layer, see (3)–(5)], this component of the response is related to the direct forcing of the SSTA.

Barotropic mode responses are shown for SSTA-0 (Fig. 5a) and SSTA-180 (Fig. 5b) experiments. They exhibit two phases of a similar pattern made of a meridional dipole of geopotential height anomalies

(A) SST−0E: Z_{Bt}
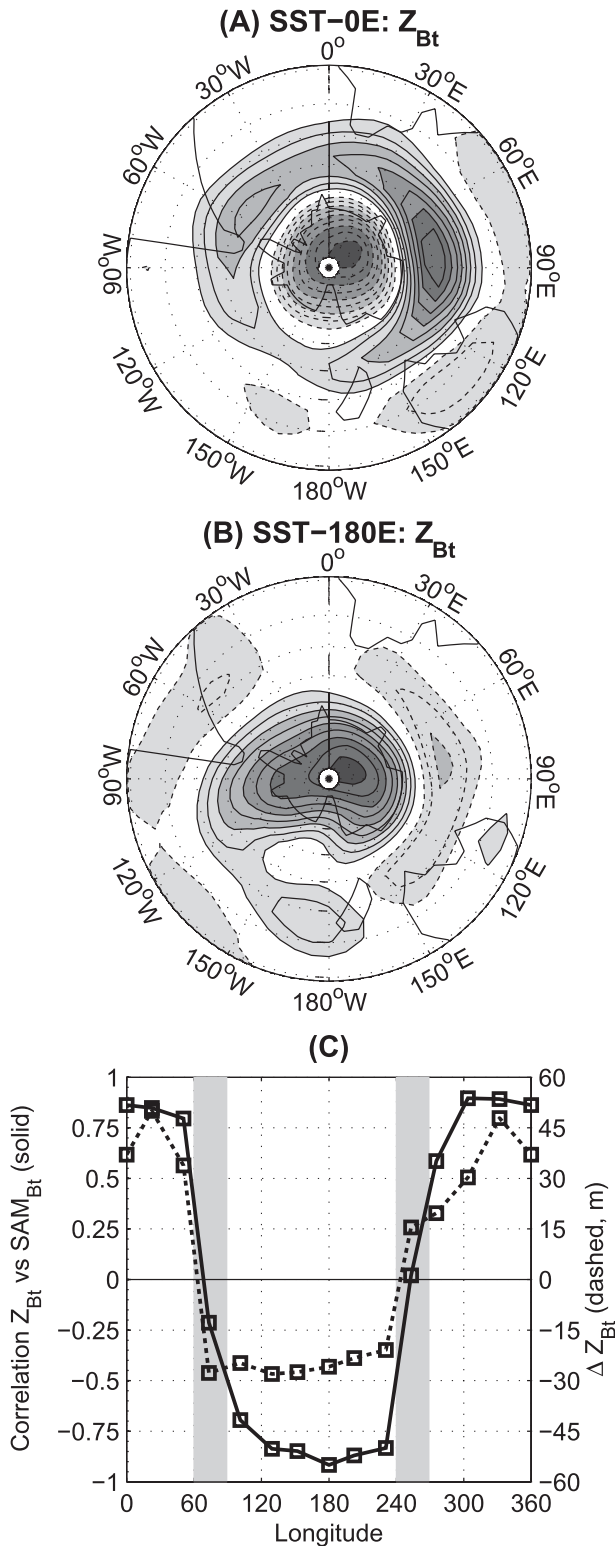
(B) SST−180E: Z_{Bt}

(C)

FIG. 5. (a),(b) Stationary atmospheric responses of geopotential height for (a) SSTA-0 and (b) SSTA-180 experiments projected on the barotropic vertical mode (Z_{Bt}). Contours are every 2 m, negative contours are dashed, the zero contour is omitted, and the shading is based on magnitude. (c) Spatial correlation coefficient

centered at midlatitudes and over the Antarctic continent. This stationary pattern is similar to the SAM (Fig. 2d).

Figure 5c illustrates how this result is persistent among the 14 experiments. It shows the spatial correlation between the barotropic mode responses and the SAM from the control simulation. Most of the correlations are greater than ±0.8 and the two bands of longitude (shaded areas) where the transition between one phase and the other occurs are remarkably narrow compared to the domain size. This curve helped to determine the two different sets of experiments introduced in the previous section and illustrated in Fig. 2a. Figure 5c also shows the meridional dipole amplitude (ΔZ_{Bt}, see figure caption). It is larger in the first set of experiments (in the range [30; 50] m), which project onto a positive SAM phase, than in the second set of experiments (in the range [−20; −30] m).

Despite a strong zonally symmetric signature, barotropic geopotential height responses also contain zonally asymmetric structures. Departures from the zonal mean of Z_{Bt} are shown in Figs. 6a,b for the SSTA-0 and SSTA-180 experiments and midlatitudes averaged for all experiments in Fig. 6c. We will refer to this component of the response as the barotropic quasi-stationary wave (QSW_{Bt}). Figure 6 shows that the QSW_{Bt} response is made of a zonal wavenumber 1 wave train propagating poleward/westward with a positive geopotential height anomaly centered 50°–60° eastward of the SSTA forcing. This pattern is remarkably persistent among the 14 experiments (Fig. 6c). It is worth noting that a low pressure anomaly at 800 hPa is not in contradiction with a local barotropic anomaly being positive. This means that the entire atmospheric air column is warming but not uniformly. Indeed, the zonal asymmetric component of the vertical average temperature response, mean of 350- and 650-hPa temperatures, is similar to the QSW_{Bt} response patterns (not shown). In the next section, we show how the QSW_{Bt} pattern is crucial to understanding the zonally symmetric response phase shift between the two sets of experiments.

←

(solid line) between Z_{Bt} responses and the control SAM_{Bt} (shown in Fig. 2d) and ΔZ_{Bt} (dashed line) for the 14 experiments as a function of SSTA forcing longitudes. For each experiment, we defined ΔZ_{Bt} as the absolute maximum minus the minimum of the Z_{Bt} response amplitude, signed with the [$Z_{Bt}SAM_{Bt}$] correlation. Thus, ΔZ_{Bt} is indicative of the meridional direction and amplitude of westerlies response shift (positive is southward; negative is northward). Shaded areas indicate the two very sharp transition regions between the two classes of responses.

(A) SST−0E: QSW$_{Bt}$

(B) SST−180E: QSW$_{Bt}$

(C) QSW$_{Bt}$ at Mid−Latitudes
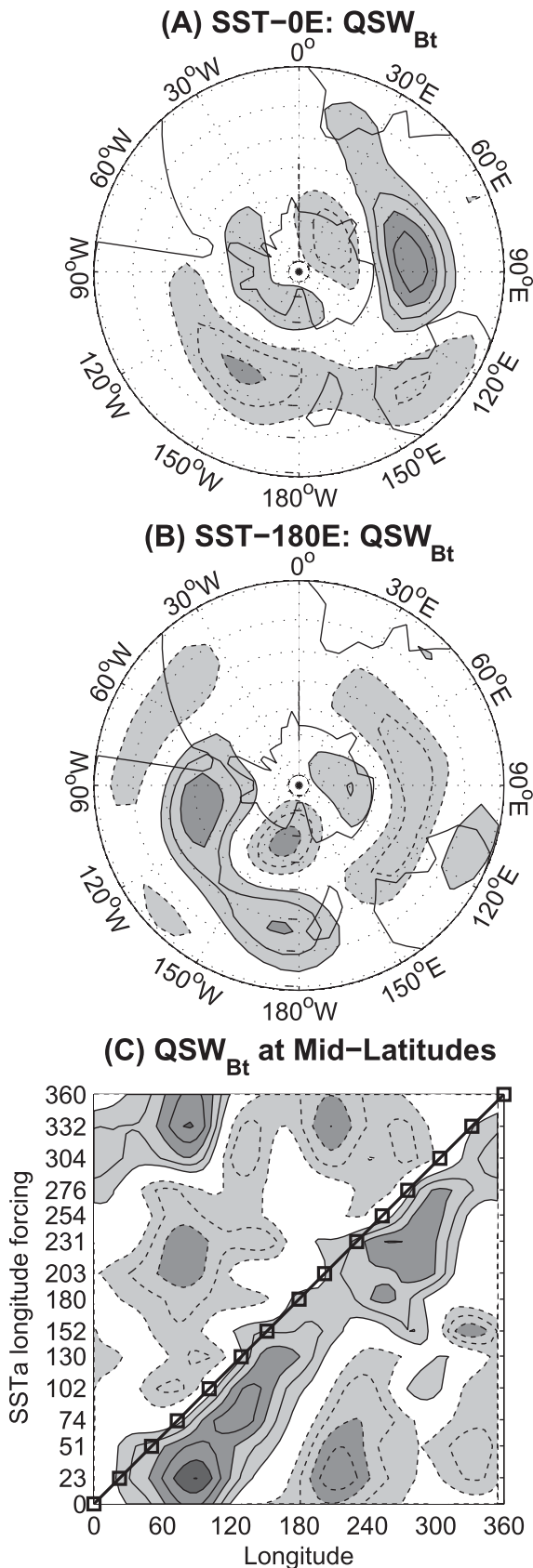
4. Potential vorticity balance leading to responses

In this section a simplified potential vorticity budget for each vertical mode of the response is conducted to understand which terms drive the PV balance and shape the stationary atmospheric responses.

Previous studies of atmospheric responses to the SSTA have shown that to understand its physical mechanism, it is crucial to separate the dynamics of transient eddies from those of quasi-stationary waves (Kushnir and Lau 1992; Kushnir et al. 2002; Ferreira and Frankignoul 2005). Consequently, we split the signal between high- and low-frequency components by use of a running mean. The cut-off frequency (the window width of the running mean) is set to 1/(7 days) and the signal decomposition is written as $q_i = q_i' + q_i^*$ and $\psi_i = \psi_i' + \psi_i^*$, where primes denote variability faster than 7 days (transient eddies) and stars denote the remaining signal. Introduced into (3)–(5) in a steady state, this leads to

$$0 = -[J(\psi_1^*, q_1^*)] - [J(\psi_1', q_1')] - [D_1] + S_1, \quad (8)$$

$$0 = -[J(\psi_2^*, q_2^*)] - [J(\psi_2', q_2')] \\ - [D_2] + [\mathcal{Q}_2] + S_2, \quad \text{and} \quad (9)$$

$$0 = -[J(\psi_3^*, q_3^*)] - [J(\psi_3', q_3')] \\ - [D_3] + [\mathcal{Q}_3] + S_3, \quad (10)$$

where [·] stands for the long-term mean, and we introduced $\mathcal{Q}_2 = -Q_{650}/K_b/R_b^2/C_{pa}$ and $\mathcal{Q}_3 = -\mathcal{Q}_2$ for readability. We note the following:

i. This set of long-term mean PV balances holds for both perturbed and control runs.

ii. Contributions from interactions between low- and high-frequency variability have been removed (even if they can be large at any time step, we verified a posteriori that their long-term mean is small compared to the other terms).

iii. The balance contains nonlinearities due to the convergence of quasi-stationary and eddy PV fluxes [first and second rhs terms in (8)–(10)] but also in the tendency due to the diabatic heating because of the

←

FIG. 6. (a),(b) QSW$_{Bt}$ responses of geopotential height for (a) SSTA-0 and (b) SSTA-180 experiments. QSW$_{Bt}$ is defined as the zonal asymmetry in the barotropic field Z_{Bt}, as those shown in Figs. 5a,b. (c) The 40°–50°S midlatitude average of QSW$_{Bt}$ as a function of longitude (x axis) and for all 14 experiments (y axis). SSTA forcing locations are indicated with black squares on the solid line. For all plots, contours are every 2 m, negative contours are dashed, the zero contour is omitted, and the shading is based on magnitude.

flow-dependent parameterization of the surface heat flux [see (6)].

Because the SSTA diabatic heating anomaly is a stretching of the lower layer, we also decomposed each PV convergence flux terms (the low- and high-frequency ones) into their relative vorticity (ζ) and vortex stretching (VS) components as follows: $J(\psi, q) = J(\psi, \zeta) + J(\psi, \text{VS})$.

These two decompositions (high versus low frequencies and relative vorticity versus vortex stretching PV convergence fluxes) multiply the number of terms to analyze at each pressure level. However, when projecting pressure-level responses onto vertical modes, the interpretation of the results is simplified because PV budgets can be reduced to a few terms. Indeed, we found that relative vorticity terms primarily project themselves onto the barotropic mode, while vortex stretching ones project themselves, naturally, onto the baroclinic modes. Thus, the anomalous form (perturbed minus control fields) of PV balances (8)–(10) projects onto vertical modes as (notice that source terms S_i cancel)

$$0 = -[J(\psi^*, \text{VS}^*)]_{\text{Bc}_1} - [J(\psi', \text{VS}')]_{\text{Bc}_1}$$
$$- [D]_{\text{Bc}_1} + [\mathcal{Q}]_{\text{Bc}_1}, \qquad (11)$$

$$0 = -[J(\psi^*, \text{VS}^*)]_{\text{Bc}_2} - [J(\psi', \text{VS}')]_{\text{Bc}_2}$$
$$- [D]_{\text{Bc}_2} + [\mathcal{Q}]_{\text{Bc}_2}, \quad \text{and} \qquad (12)$$

$$0 = -[J(\psi^*, \zeta^*)]_{\text{Bt}} - [J(\psi', \zeta')]_{\text{Bt}} - [D]_{\text{Bt}} + H_{\text{Bt}}, \quad (13)$$

where vertical-mode interaction terms are as follows:

1) Omitted in both baroclinic modes because we found a posteriori that they are unnecessary to the first-order PV budget we want to investigate here and

2) Represented by the new term H_{Bt} in the barotropic mode. This term is necessary because it is the only way for the SSTA to influence the barotropic mode in this three-layer model, where surface heat sources are localized in the lower layer only. The term H_{Bt} primarily represents baroclinic mode interactions (the vertical propagation of anomalies).

Finally, (11)–(13) are interpreted as an equilibrium between forcing and response terms, which are, in turn, balanced by a damping—to ensure a closed and zero PV budget. In the following two subsections, we will focus on the forcing/response terms equilibria, the one inducing a PV tendency responsible for geopotential height anomalies.

a. PV balance of baroclinic modes

Special attention needs to be paid to the heat flux term $\mathcal{Q}$ and therefore Q_{650} and F. The anomalous air–sea heat flux is a nonlinear combination of surface temperature and wind amplitude anomalies. These are, in turn, made of a direct forcing and an atmospheric response component. Using such a decomposition in surface variables would result in multiple heat flux components difficult to relate to a simple forcing/response equilibrium. Instead, we used a heat flux decomposition of the form

$$[F] = [F^{\text{SST}}] + [F^{\text{ATM}}], \qquad (14)$$

where $[F^{\text{SST}}]$ is the forcing component induced by the SSTA and $[F^{\text{ATM}}]$ is the heat flux induced by atmospheric responses in surface temperature and wind. An estimate of the heat flux forcing term $[F^{\text{SST}}]$ is obtained using mean fields of sea surface atmospheric air temperature and wind amplitude from the control simulation and SST fields with and without anomalies.

The $[F^{\text{ATM}}]$ term is simply computed as the difference between the two other terms. It is a second-order term in the main forcing/response balance, in a sense that it is induced indirectly by the SSTA through the effect of the atmospheric response. In other words, it is a consequence of the initial atmospheric response instead of the direct SSTA forcing. The $[F^{\text{ATM}}]$ term is driven by positive temperature anomalies in the lower layer (see Figs. 3e–j). It is therefore negative (warming the ocean) and very close in shape to T (650 hPa) (not shown). It has a 14-experiment ensemble mean of -5 W m^{-2} (corresponding to a heating rate of -0.10 K day^{-1} at 650 hPa) with values between -10 and -3 W m^{-2} in the western Pacific Ocean and Atlantic–western Indian Oceans (the heating rate is between -0.19 and -0.06 K day^{-1}). In a coupled model, this component of the heat flux anomaly would help sustain the SSTA and increase its persistence. This is indeed what was shown by M06. Here it tends to moderate the amplitude of the direct atmospheric response, reducing the stretching between layers, and it will therefore be omitted.

Using (14) to decompose heat sources at pressure level $\mathcal{Q}_{2,3} = \pm Q_{650}/K_b/R_b^2/C_{\text{pa}}$ and for baroclinic modes $[\mathcal{Q}]_{\text{Bc}_i}$, we can write

$$[\mathcal{Q}^{\text{SST}}]_{\text{Bc}_i} - [J(\psi^*, \text{VS}^*)]_{\text{Bc}_i} - [J(\psi', \text{VS}')]_{\text{Bc}_i} \propto [q_{\text{Bc}_i}]$$
$$(15)$$

for $i = 1, 2$ and where $[q]_{\text{Bc}_i}$ are the baroclinic PV responses shown as geopotential heights in Fig. 4. All lhs terms of (15) and their sum are shown for experiments SSTA-0 (left columns) and SSTA-180 (right columns) in Fig. 7 for baroclinic mode 1 and Fig. 8 for baroclinic mode 2. We now describe these patterns.

The baroclinic heat source forcing $[\mathcal{Q}^{\text{SST}}]_{\text{Bc}_i}$ has the SSTA pattern, but it sees its amplitude varying according
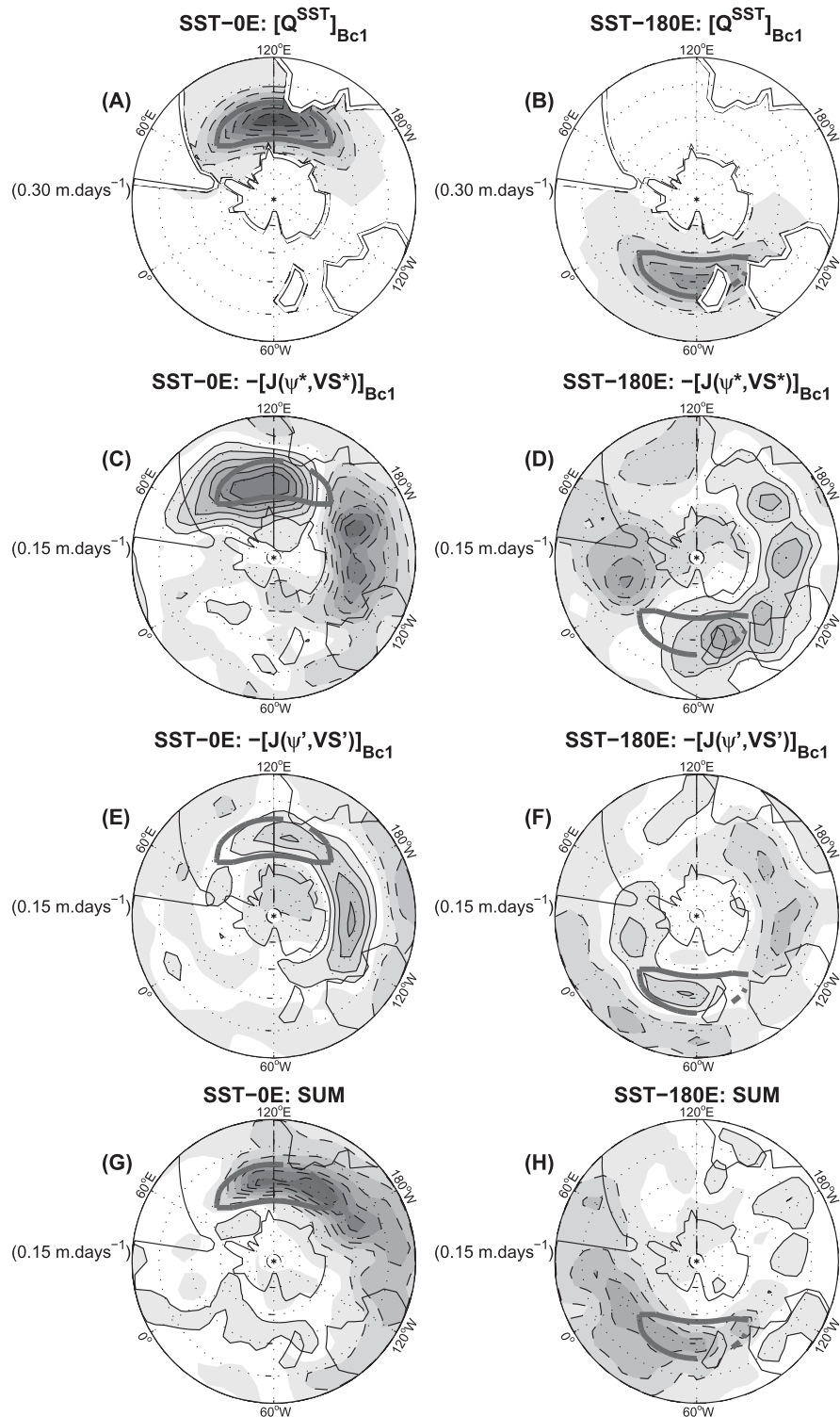
FIG. 7. First baroclinic mode anomalous PV budget terms, lhs of (15), for experiments (left) SSTA-0 and (right) SSTA-180. (a),(b) Heat flux term due to the direct forcing of the SSTA: $[\mathcal{Q}^{SST}]_{Bc_1}$. (c),(d) PV tendency due to the quasi-stationary vortex stretching flux: $-[J(\psi^*, VS^*)]_{Bc_1}$. (e),(f) PV tendency due to the eddy vortex stretching flux: $-[J(\psi^*, VS^*)]_{Bc_1}$. (g),(h) Sum of the three terms; responsible for the baroclinic mode response shown in Figs. 4a–d. All PV tendencies are plotted as geopotential height tendencies with negative contours dashed, zero contours omitted, with the contours increment indicated to the left of each plot and shading based on magnitude. Locations of SSTAs are indicated by a thick gray line.

SST−0E: $[Q^{SST}]_{Bc2}$

SST−180E: $[Q^{SST}]_{Bc2}$

(A)

(B)

(0.30 m.days^{-1})

(0.30 m.days^{-1})

SST−0E: $-[J(\psi^*, VS^*)]_{Bc2}$

SST−180E: $-[J(\psi^*, VS^*)]_{Bc2}$

(C)

(D)

(0.20 m.days^{-1})

(0.20 m.days^{-1})

SST−0E: $-[J(\psi', VS')]_{Bc2}$

SST−180E: $-[J(\psi', VS')]_{Bc2}$

(E)

(F)

(0.20 m.days^{-1})

(0.20 m.days^{-1})

SST−0E: SUM

SST−180E: SUM

(G)

(H)

(0.20 m.days^{-1})
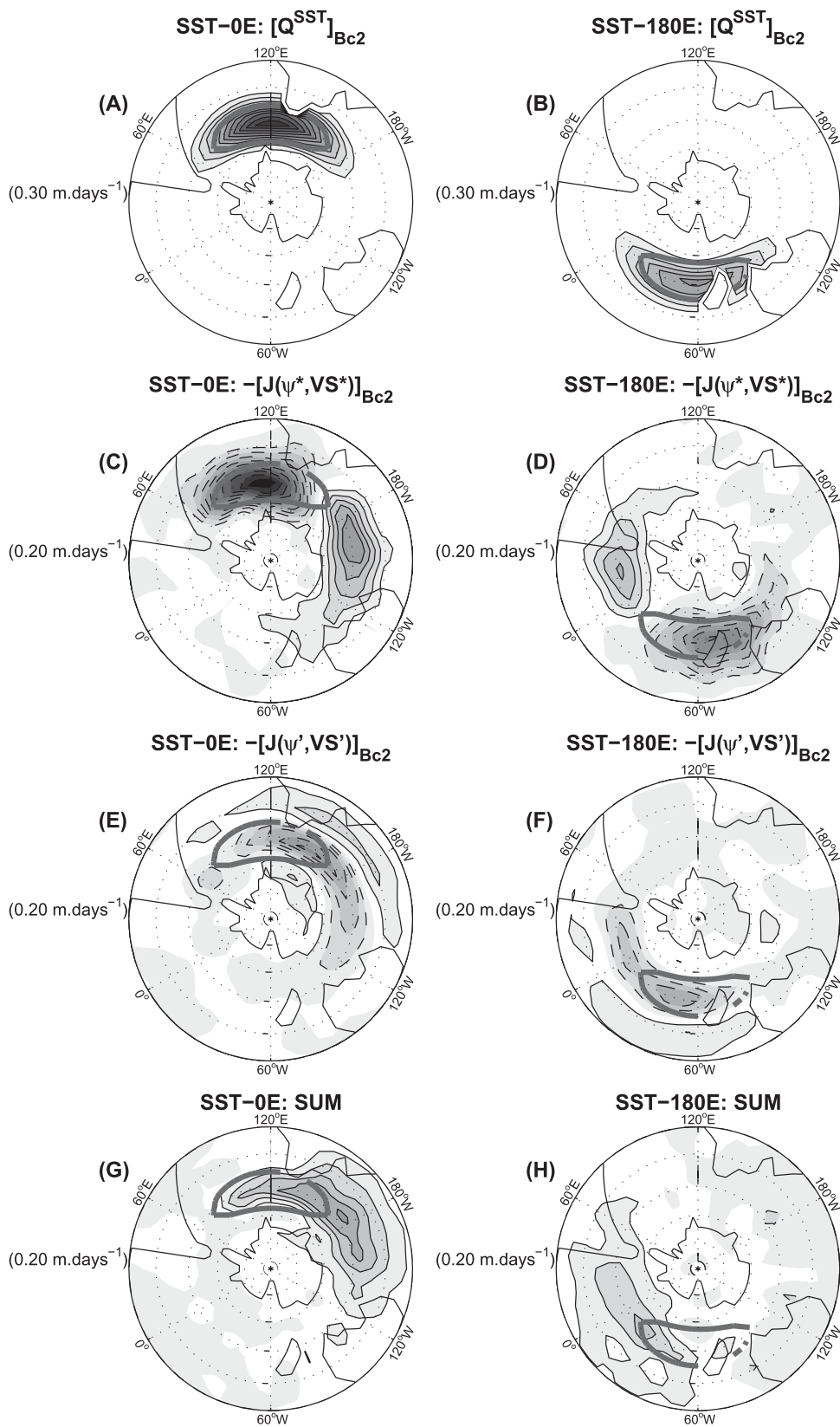
(0.20 m.days^{-1})

FIG. 8. As in Fig. 7, but for the second baroclinic mode, lhs terms of (15).

to zonal asymmetries in surface atmospheric fields. It has a 14-experiment ensemble mean amplitude of 24 W m^{-2} (and a corresponding heating rate at 650 hPa of 0.45 K day^{-1}) with values between 15 and 31 W m^{-2} (the heating rate is between 0.28 and 0.59 K day^{-1} at 650 hPa) in the western Pacific Ocean and Atlantic–western Indian Oceans.

The baroclinic quasi-stationary vortex stretching flux $-[J(\psi^*, VS^*)]_{Bc_i}$ exhibits a zonal dipole in the midlatitude band, centered ∼30° downstream of the SSTA center, reminiscent of an advective pattern. The negative (positive) vortex stretching anomaly induced by the SSTA in the first (second) baroclinic mode is clearly advected eastward by the quasi-stationary flow. Contributions from the stationary flow are dominant upon the low-frequency one in this advection pattern (not shown). Like geopotential height responses, their amplitudes are larger in the SSTA-0 case than in the SSTA-180 case. And not surprisingly, these tendency patterns are very similar among the 14 experiments with regard to their relative positions to the SSTA forcing longitude.

The baroclinic high-frequency eddy vortex stretching flux $-[J(\psi', VS')]_{Bc_i}$ is of the opposite sign of the vortex stretching anomaly at the latitude of the SSTA forcing and of the same sign north and southward of it, with a relatively small zonal asymmetry. This term thus plays a dissipative role in the balance. It dissipates in the meridional direction the anomalous vortex stretching induced by the SSTA and again, no differences are found between experiments except in the amplitude. The anomalous vortex stretching induced by the SSTA increases the available potential energy of the atmospheric column, which tends to be released through baroclinic instability, that is, by an increase of the baroclinic transients activity. They induce a divergence of eddy temperature flux in the latitude band of the SSTA and a convergence on its north–south flanks, which explains the pattern of $-[J(\psi', VS')]_{Bc_i}$.

The sum of all terms shows a geopotential height tendency pattern close to the baroclinic responses shown in Fig. 4. The warm atmospheric temperature response, shifted eastward from the SSTA forcing longitude, is well explained by a simple equilibrium between the SSTA direct forcing and (i) advection from the quasi-stationary flow and (ii) dissipation by the high-frequency transient eddies. This balance holds in the vicinity of the SSTA, from its longitude center up to 90° eastward. For the 14 experiments, we observed baroclinic responses similar with regard to their relative distribution to the SSTA forcing position. This is also true for the baroclinic PV balance terms shaping the response pattern. However, the simplified PV budget of the first baroclinic mode is not able to explain the

different sign of the geopotential height anomalies observed over the South Pole in the experiments SSTA-0 and SSTA-180. Such a discrepancy from the budget and the observed responses probably arises from the error accumulation of all decompositions.

b. PV balance of the barotropic mode

The barotropic PV budget (13) is quantitatively harder to tackle than the baroclinic ones because of the unknown forcing term H_{Bt}. Although the baroclinic modes are almost directly forced by the SSTA—and a direct diagnostic is possible—the barotropic mode response necessarily involves the integrated (both vertically and over time) effect of the vertical propagation of anomalies. This is simply because the vertical integral of the discretized heat sources in (3)–(5) is zero. Thus, the barotropic response must be forced by anomalies in surface boundary conditions diagnosed from anomalous baroclinic heat sources. We choose not to conduct this diagnostic of H_{Bt} because it involves multiple complicated and convoluted scalings to transform the vertically averaged atmospheric temperature response into an anomalous surface heat flux suited for a barotropic atmosphere. However, we show hereafter that a qualitative discussion of H_{Bt} with an analysis of the other terms from (13) is satisfactory enough to explain the pattern and behavior of the atmospheric barotropic responses. In other words, in this sequence of experiments, the qualitative knowledge of the forcing is sufficient to understanding the forcing/response equilibria.

In section 3 we show that the lower and upper layers of the atmosphere warm eastward of the SSTA [see Fig. 4 and (B5), for instance]. This reflects a warming of the entire air column—a barotropic warm-air anomaly—although not with a uniform distribution along the vertical axis. When this warming projects at the surface, it modifies the boundary conditions of the equivalent barotropic atmosphere and can force the barotropic mode response. More precisely, here it forces a local downstream high pressure anomaly (because the entire air column warming makes geopotential height surfaces move upward), which in turn excites a planetary Rossby wave train. This is indeed what is seen in the barotropic quasi-stationary wave responses (Fig. 6). The QSW$_{Bt}$ atmospheric response turns out to be a proxy of the H_{Bt} forcing pattern and is induced by a simple local warming of the entire air column.

How then can the different projections on the SAM phase be explained?

Figure 9 shows zonal anomalies of $-[J(\psi^*, \zeta^*)]_{Bt}$ and $-[J(\psi', \zeta')]_{Bt}$ for the SSTA-0 and SSTA-180 experiments. We can see that the high pressure anomaly from the barotropic forcing term H_{Bt} is (i) balanced by a low
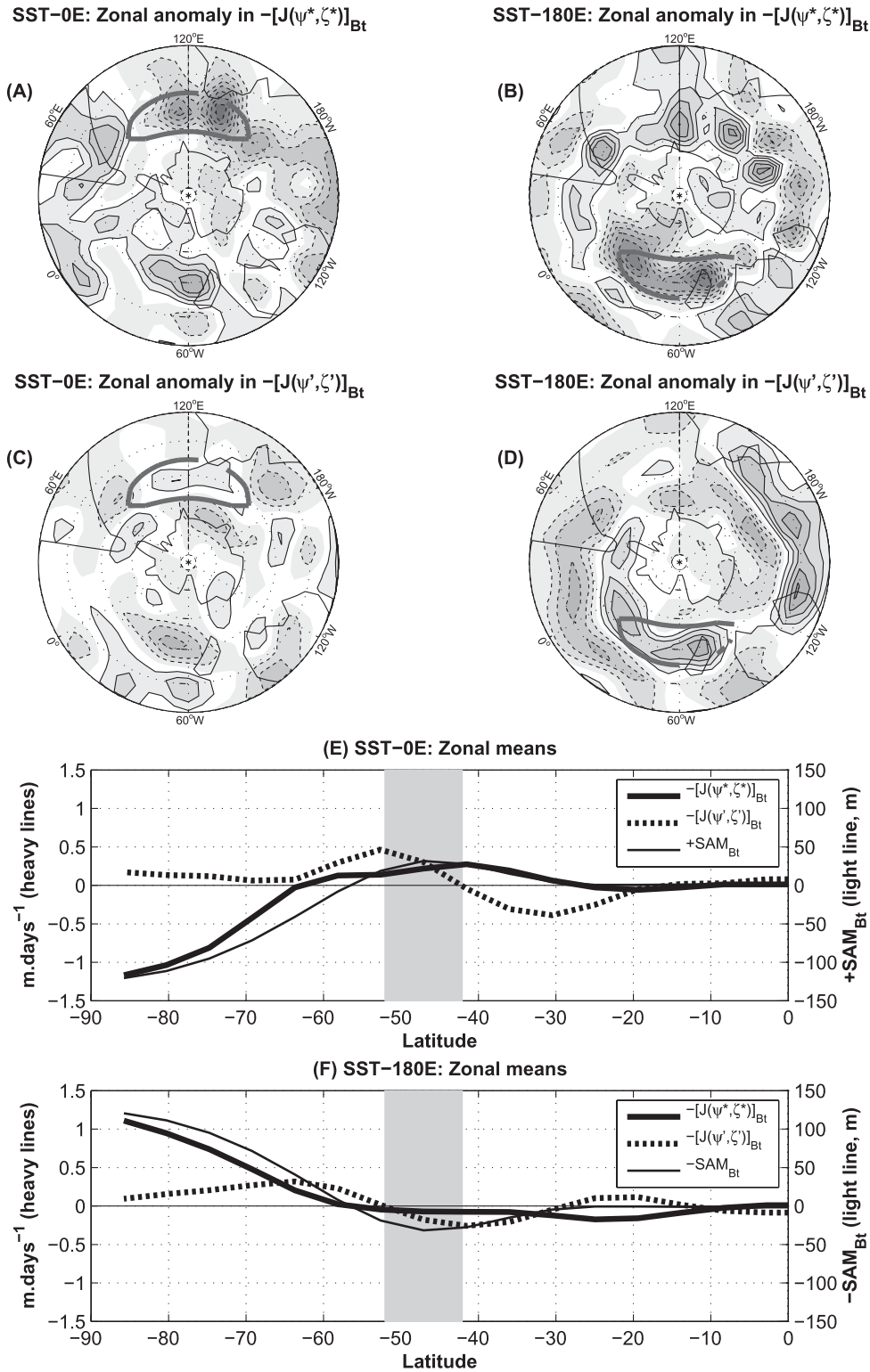
FIG. 9. (a)–(d) Zonal anomalies in the (first row) low-frequency and (second row) high-frequency relative vorticity fluxes for experiments (left) SSTA-0 and (right) SSTA-180—first and second rhs terms of (13). Contours are every 0.25 m day^{-1}, the zero contour is omitted, negative contours are dashed, and the shading is based on magnitude. Locations of SSTAs are indicated by a thick gray line. Zonal means of the low-frequency (solid) and high-frequency (dashed) relative vorticity fluxes for experiments (e) SSTA-0 and (f) SSTA-180. Zonal mean of SAM$_{Bt}$ in a positive (negative) phase is also plotted in (e) [(f)] as a thin solid line. SSTA forcing latitude band is highlighted by the gray-shaded area.

(A) Initial forcing phase: **(B) Stationary response:**   **(C) Stationary response:**
                                                                     vertical mean, zonal anomaly

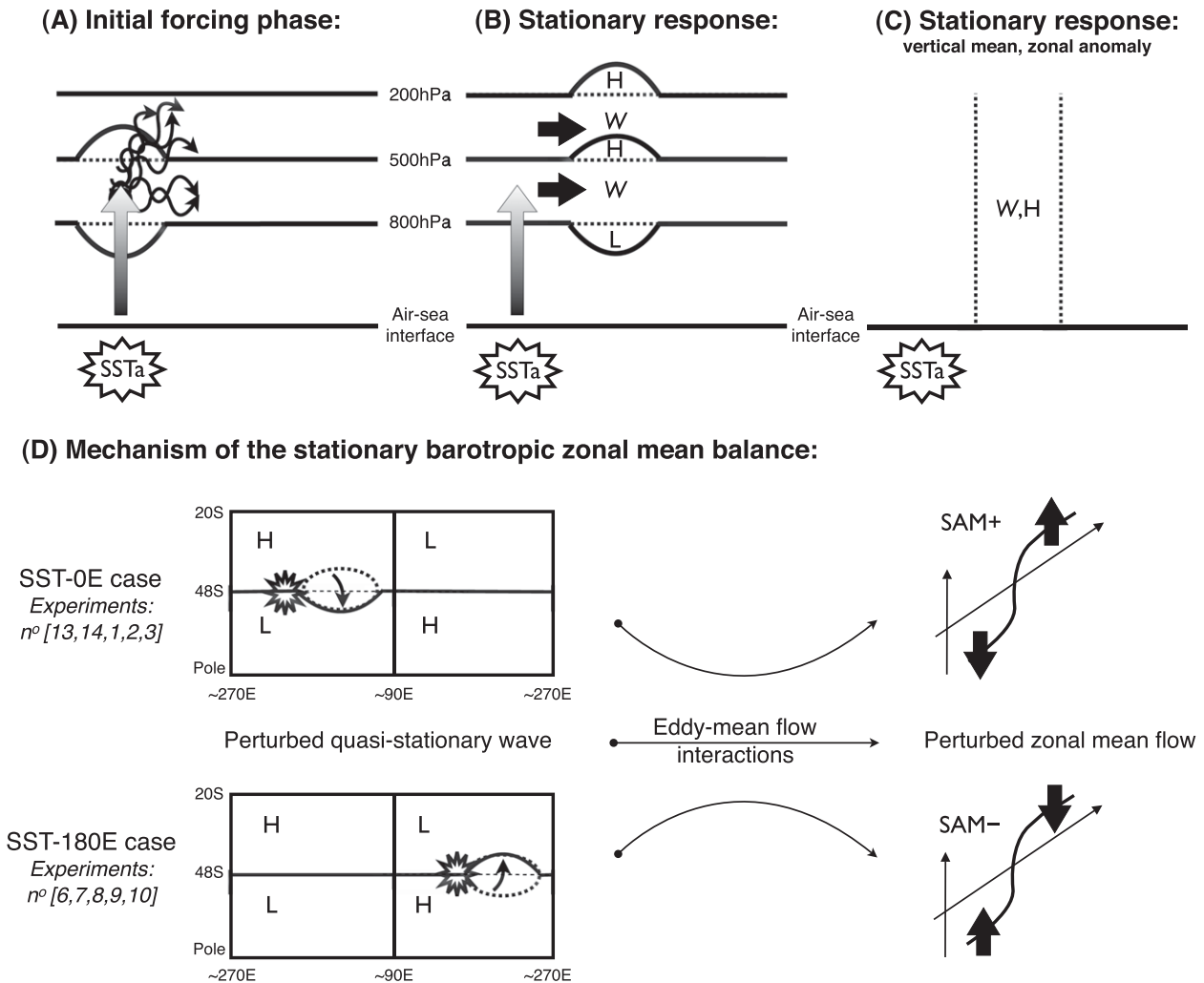**(D) Mechanism of the stationary barotropic zonal mean balance:**

FIG. 10. (a) Initial forcing phase of the response with SSTA anomalous heat flux (shaded vertical arrow) inducing a stretching of the lower layer (geopotential heights in solid/dashed black lines), which in turn triggers baroclinic instability (curvy thin arrows). (b) Main local balance between heat flux forcing and advection of stretching by the quasi-stationary flow (plain black horizontal arrows). Meridional damping by eddies not shown. Symbols "W" and "H/L" denote warm air and high/low pressure anomalies, respectively. (c) Zonal anomaly of the barotropic response with a barotropic high pressure and warm-air anomaly downstream of the SSTA. (d) Left is a schematic view of the horizontal QSW_{Bt} unperturbed field (see Fig. 2c) with a succession of highs and lows zonally and meridionally. Superimposed are the SSTA forcing location (black star) and the QSW_{Bt} high pressure response (dashed ellipse). This perturbation of the climatological quasi-stationary wave pattern interacts with the zonal-mean flow through the relative vorticity flux to shift the maximum latitude of the westerlies (positive and negative phases of the SAM) southward/northward.

pressure anomaly induced by the convergence of quasi-stationary relative vorticity fluxes (Figs. 9a,b) and (ii) slightly reinforced by the eddy component of the relative vorticity flux (Figs. 9c,d). For all 14 experiments, these patterns of zonal anomalies are phase locked with the SSTA forcing longitude, similar to the QSW_{Bt} responses.

The zonal mean of $-[J(\psi^*, \zeta^*)]_{Bt}$ and $-[J(\psi', \zeta')]_{Bt}$ are shown in Figs. 9e,f. The eddy ζ flux (thick dashed line) is negligible over the South Pole and made of a dipole at midlatitudes with a convergence to the south

and a divergence to the north of the SSTA latitude, simply revealing an extremum of high-frequency eddy structures at this latitude. For experiment SSTA-0 (Fig. 9e), the quasi-stationary ζ flux (thick solid line) is a meridional dipole with large negative (positive) values over the South Pole (at midlatitudes), which compare well to the meridional structure of the SAM_{Bt} zonal mean in a positive phase and to the Z_{Bt} zonal-mean response (not shown but illustrated in Fig. 5). For experiment SSTA-180 (Fig. 9f), we observe a similar structure and correlation with a negative phase of the SAM_{Bt}.

This is evidence that $-[J(\psi^*, \zeta^*)]_{Bt}$ drives the sign of the geopotential height response projection on the SAM_{Bt} pattern. Indeed, the low-frequency eddy–mean flow interaction process, here captured by the $-[J(\psi^*, \zeta^*)]_{Bt}$ term, is partially responsible for the meridional structure of the zonal-mean zonal velocity field ($\partial_t u \propto -\partial_v u^* v^*$). Zonal asymmetries in the time-mean flow arise from zonal anomalies in surface boundary conditions. As one can see from Fig. 2c, the control quasi-stationary wave pattern has a zero contour at the SSTA forcing latitude flanked to the north/south of (i) high/low pressure anomalies from Drake Passage to the western Indian Ocean and (ii) low/high pressure anomalies from south of Australia to the mid-Pacific Ocean. The downstream high pressure anomaly from the QSW_{Bt} response thus modifies the meridional high/low pressure distribution of the control wave (shifting the control high pressure anomaly south or northward) and hence the meridional structure of the zonal-mean flow through low-frequency relative vorticity fluxes. Having zonal asymmetries in the control state and a perturbed low-frequency eddy field locked with the SSTA forcing longitude induces the possibility for the perturbed flow to reinforce or weaken eddy–mean flow interactions and to project responses onto positive/negative phases of the dominant zonal-mean flow pattern.

5. Discussion

An analysis of 14 experiments where an atmospheric QG model was forced by an idealized SSTA centered at midlatitudes and 14 different longitudes was presented. We focused on the vertical structures of stationary responses by projecting pressure-level anomalies onto the three vertical modes of the model. One obtained a barotropic component and two baroclinic modes, representing the vertical distribution of layer stretching. Results are illustrated by schematics in Fig. 10.

We found that the two baroclinic modes and the zonal anomaly of the barotropic one (QSW_{Bt}) are insensitive to the SSTA location, in the sense that they are zonally phase locked with the SSTA forcing position. Conversely, zonal average responses show a SAM-like pattern with a phase highly sensitive to the SSTA location: positive for a forcing centered from the Drake Passage to the western Indian Ocean and negative for a forcing centered between south of Australia and the mid-Pacific Ocean.

Baroclinic modes anomalies—warm-air anomalies in the lower and upper layers—have basically the SSTA forcing pattern shifted downstream, eastward, by ~40°–50° (Fig. 4). These types of baroclinic responses have long been observed in the North Atlantic and the North Pacific regions (Ting and Peng 1995; Peng and Whitaker 1999). Their dynamical balance is schematically illustrated in Figs. 10a,b. Using an approximated potential vorticity budget, we determined that baroclinic responses can largely be explained by the anomalous vortex stretching induced by the SSTA being balanced by (i) advection by the quasi-stationary flow (dominated by the stationary part, not shown) and (ii) dissipation by the mean transient effect. We also determined that the amplitude of these baroclinic mode structures is linearly proportional to the SSTA amplitude for anomalies up to ±4°C (not shown), with the lower-layer atmospheric temperature anomaly about 70% of the SSTA amplitude. We did not compare our results to a classic linear baroclinic model experiment (e.g., Peng et al. 2003), but these elements seem to agree with the linear QG theory (Smagorinsky 1953; Hoskins and Karoly 1981; Frankignoul 1985).

Although the heat anomaly is not uniformly distributed throughout the vertical, all stationary responses show a warming of the entire air column 40°–50° downstream of the SSTA (Fig. 10c). This barotropic warming induces a high pressure anomaly simply through rising geopotential height surfaces, which in turn excite a barotropic quasi-stationary Rossby wave train propagating poleward/westward and of zonal wavenumber 1 (see Fig. 6). The amplitude of the QSW_{Bt} response, from 4 to 10 m, is about 10% of the amplitude of the control field (from 60 m at midlatitudes to 100 m around the South Pole). It is worth noting that having a downstream low pressure anomaly response at 800 hPa—and one would expect a similar surface pressure response—is not in contradiction with a barotropic downstream high pressure anomaly.

The simplified control QSW_{Bt} pattern is schematically represented in Fig. 10d (see Fig. 2c for more details). It has a zero contour at the SSTA forcing latitude flanked to the north/south of (i) high/low pressure anomalies from Drake Passage to the western Indian Ocean and (ii) low/high pressure anomalies from south of Australia to the mid-Pacific Ocean. The sensitivity of the zonal-mean response phase to the SSTA forcing position is due to this pattern. Indeed, the downstream high pressure anomaly from the QSW_{Bt} response modifies the meridional high/low pressure distribution in opposite ways, depending on where the SSTA forcing is localized (see Fig. 10d for the SSTA-0 and SSTA-180 experiments). Diagnosing low- and high-frequency relative vorticity eddy fluxes, we have shown that it is the low-frequency eddy component that is responsible for the modified eddy–mean flow interaction leading to different responses.

In reality the high-frequency eddy component plays a very significant role in eddy–mean flow interactions of the Southern Hemisphere (see Watterson 2002, for

instance). It is possible that we obtained this result be-cause the bottom friction time scale used in the model (from 1.5 to 3 days, depending on topography) is too short compared to the observations [Watterson (2007), found 8.6 days as an effective time] and hence high-frequency eddies are damped too quickly. If the damp-ing is decreased (i.e., with a longer time scale), then the model should also produce responses less localized to the forcing, with stronger eastward propagation and with larger amplitudes, which could alter the low-frequency/high-frequency eddy interactions with the mean flow. Seasonality may also play a role even if the observed damping time scales are shorter in winter—the season modeled here—than in summer (Watterson 2002).

Finally, it is remarkable that we obtained such a simple zonal-mean response behavior with respect to the SSTA forcing position (same pattern, two phases). Our study suggests that a warming of the midlatitudes Southern Ocean is likely to have two opposite impacts on the SAM, depending on the warming position: positive for Atlantic Ocean to western Indian Ocean warming and negative for south of Australia to mid-Pacific Ocean warming. As a consequence, this also suggests that it may be possible to enhance a trend in the SAM through the warming of dis-tinct regions of the Southern Ocean.

6. Conclusions

Using a three-level quasigeostrophic atmospheric model forced by the ocean through a diabatic heat source in the lower layer, we determined the stationary atmospheric response to an idealized SST anomaly in the Southern Ocean in perpetual winter conditions. Although in many past studies, atmospheric responses to SST anomalies had been analyzed in simple zonally symmetric models mimicking the Southern Hemisphere (e.g., Inatsu et al. 2003; Ring and Plumb 2007), this study takes into account asymmetries, both in the high-frequency and low-frequency atmospheric variability (storm track and quasi-stationary eddies). This study suggests that these asymmetries play a crucial role, albeit small compared to their Northern Hemisphere counterpart, in determining the large-scale atmospheric response to a SST anomaly in the Southern Hemisphere.

Further investigations are needed to check the ro-bustness of these results in more complex atmospheric models. In particular, it is necessary to clarify the influence of (i) the friction parameterization, using different dissi-pation time scales, both in the bottom friction and the layer radiative coupling; (ii) the background state and especially the seasonality of the quasi-stationary wave pattern; and (iii) the vertical profile of the heat source, extending the vertical penetration of heat to the upper layer.

To conclude, we have shown that a SSTA transported by the ACC can impact the overlying atmosphere. Baroclinic and barotropic zonal anomalies responses are phased locked with the SSTA forcing position, shifted down-stream by ~50°. These responses could feed back onto the SSTA through anomalous zonal winds modifying oceanic currents and/or air–sea fluxes.

And finally, we also have shown that the SAM is sensitive to midlatitudes SSTAs. The zonal-mean baro-tropic response is either reinforcing or weakening a SAM-like pattern, depending on the localization of the SSTA forcing with respect to the control quasi-stationary wave. Whether midlatitude Southern Ocean warming trends [as those observed by Gille et al. (2001), for in-stance] could contribute to the observed SAM trend will require complementary studies using more realistic mod-els. Our study, with caution, suggests that the midlatitudes Southern Ocean may also play a role in driving climatic trends in the Southern Hemisphere atmosphere.

APPENDIX A

Source Terms

The usual way to compute source terms S_i in PV equations gives better results when applied to South-ern Hemisphere when corrected with a fixed temper-ature profile. This term was computed in the following way.

The Marshall and Molteni (1993) forcing term S_i can be interpreted as a relaxation temperature in the sense of Held and Suarez (1994). Equations (3)–(5) can in fact be obtained by eliminating the vertical velocity ω in the QG vorticity and temperature equations (cf. Holton 1992, p. 164) as T^* follows:

$$\frac{d\nabla^2\psi}{dt} = f_0\frac{\partial\omega}{\partial p} \quad \text{and} \tag{A1}$$

$$f_0\frac{d\psi}{dt} = -\sigma\omega + F(\psi, T) + \frac{R}{p}\frac{1}{\tau}(T^* - T), \tag{A2}$$

which gives

$$\frac{Dq}{Dt} = \frac{f_0}{\sigma}\frac{\partial}{\partial p}F(\psi,T) - \frac{f_0}{\sigma}\frac{1}{\tau}\frac{\partial}{\partial p}\left[\frac{R}{p}T\right] + \frac{f_0}{\sigma}\frac{1}{\tau}\frac{\partial}{\partial p}\left[\frac{R}{p}T^*\right]. \quad (A3)$$

Here, q is the potential vorticity, ψ is the geostrophic streamfunction, f_0 is the Coriolis factor at 45°S, σ is the static stability, R is the gas constant, and τ is a relaxation time scale. The first term on the rhs of (A3) corresponds to the heat flux term in (4) and (5). The second term on the rhs of (A3) corresponds to the dissipation term of (3)–(5). Finally, the third term represents the Held and Suarez (1994) relaxation temperature.

The Marshall and Molteni (1993) forcing method, in other terms, can be seen as an empirical way to compute a relaxation temperature T^*.

To correct the forcing term S, we added a zonally uniform temperature $T^{*\prime}$ and recomputed a new term, S', as follows:

$$S' = \frac{f_0}{\sigma}\frac{1}{\tau}\frac{\partial}{\partial p}\left[\frac{R}{p}(T^*+T^{*\prime})\right], \quad (A4)$$

where $T^{*\prime}$ is pretty much an ad hoc term. It was computed as a fraction of the difference in the meridional profile between T^* and the observed meridional temperature profile.

APPENDIX B

Vertical Modes

Because the model is discretized at three pressure levels, it can be projected onto three vertical modes: one barotropic and two baroclinic. These are defined as the eigenvectors of the transfer matrix $\mathbf{T}$, defined by the vortex stretching term of the transformation of the streamfunctions ψ into the potential vorticities q:

$$\begin{pmatrix} q_{200} \\ q_{500} \\ q_{800} \end{pmatrix} = \mathbf{T}\begin{pmatrix} \psi_{200} \\ \psi_{500} \\ \psi_{800} \end{pmatrix}, \quad (B1)$$

where $\mathbf{T}$ is defined as

$$\mathbf{T} = \begin{pmatrix} -\dfrac{1}{R_h^2} & \dfrac{1}{R_h^2} & 0 \\ \dfrac{1}{R_h^2} & -\dfrac{1}{R_h^2} - \dfrac{1}{R_b^2} & \dfrac{1}{R_b^2} \\ 0 & \dfrac{1}{R_b^2} & -\dfrac{1}{R_b^2} \end{pmatrix}, \quad (B2)$$

with $R_h = 700$ km and $R_b = 450$ km as the Rossby radius of deformation of the upper and lower layers of the model (see Fig. 1). Then vertical modes of a variable

defined at each pressure level (potential vorticity, streamfunction, or geopotential height z) are obtained through the inversion of

$$\begin{pmatrix} z_{200} \\ z_{500} \\ z_{800} \end{pmatrix} = \mathbf{M}\begin{pmatrix} z_{Bt} \\ z_{Bc_1} \\ z_{Bc_2} \end{pmatrix}, \quad (B3)$$

where indices Bt, Bc_1, and Bc_2 denote the barotropic, and the first and second baroclinic modes, and the matrix $\mathbf{M}$ contains the eigenvectors of the transfer matrix $\mathbf{T}$. This can be numerically approximated by

$$\begin{pmatrix} z_{Bt} \\ z_{Bc_1} \\ z_{Bc_2} \end{pmatrix} \simeq \begin{pmatrix} 0.57 & 0.57 & 0.57 \\ -0.79 & 0.25 & 0.54 \\ -0.17 & 0.77 & -0.6 \end{pmatrix}\begin{pmatrix} z_{200} \\ z_{500} \\ z_{800} \end{pmatrix}. \quad (B4)$$

Note that given the thermal wind relation in each layers, vertical baroclinic modes of geopotential height may be related to temperatures at 350 and 650 hPa through

$$\begin{pmatrix} z_{Bc_1} \\ z_{Bc_2} \end{pmatrix} \simeq \begin{pmatrix} -21.41 & -7.54 \\ -4.60 & 8.33 \end{pmatrix}\begin{pmatrix} T_{350} \\ T_{650} \end{pmatrix}. \quad (B5)$$

REFERENCES

Butler, A. H., D. W. J. Thompson, and R. Heikes, 2010: The steady-state atmospheric circulation response to climate change–like thermal forcings in a simple general circulation model. *J. Climate*, **23**, 3474–3496.

Codron, F., 2007: Relations between annular modes and the mean state: Southern Hemisphere winter. *J. Atmos. Sci.*, **64**, 3328–3339.

Connolley, W., 2002: Long-term variation of the Antarctic circumpolar wave. *J. Geophys. Res.*, **107**, 8076, doi:10.1029/2000JC000380.

Czaja, A., and C. Frankignoul, 2002: Observed impact of Atlantic SST anomalies on the North Atlantic Oscillation. *J. Climate*, **15**, 606–623.

D'Andrea, F., and R. Vautard, 2000: Reducing systematic errors by empirically correcting model errors. *Tellus*, **52A**, 21–41, doi:10.1034/j.1600-0870.2000.520103.x.

——, A. Czaja, and J. Marshall, 2005: Impact of anomalous ocean heat transport on the North Atlantic Oscillation. *J. Climate*, **18**, 4955–4969.

Ferreira, D., and C. Frankignoul, 2005: The transient atmospheric response to midlatitude SST anomalies. *J. Climate*, **18**, 1049–1067.

——, and ——, 2008: Transient atmospheric response to interactive SST anomalies. *J. Climate*, **21**, 576–583.

Frankignoul, C., 1985: Sea surface temperature anomalies, planetary waves, and air-sea feedback in the middle latitudes. *Rev. Geophys.*, **23**, 357–390.

Gibson, R., P. Kållberg, and S. Uppala, 1996: The ECMWF Reanalysis (ERA) project. *ECMWF Newsletter*, No. 73, ECMWF, Reading, United Kingdom, 7–17.

Gille, S. T., D. P. Stevens, R. T. Tokmakian, and K. J. Heywood, 2001: Antarctic Circumpolar Current response to zonally averaged winds. *J. Geophys. Res.,* 106, 2743–2759.

Gillett, N. P., and D. W. J. Thompson, 2003: Simulation of recent Southern Hemisphere climate change. *Science,* 302, 273–275.

Grassi, B., G. Redaelli, and G. Visconti, 2005: Simulation of polar Antarctic trends: Influence of tropical SST. *Geophys. Res. Lett.,* 32, L23806, doi:10.1029/2005GL023804.

Hall, A., and M. Visbeck, 2002: Synchronous variability in the Southern Hemisphere atmosphere, sea ice, and ocean resulting from the annular mode. *J. Climate,* 15, 3043–3057.

Hall, N. M. J., J. Derome, and H. Lin, 2001: The extratropical signal generated by a midlatitude SST anomaly. Part I: Sensitivity at equilibrium. *J. Climate,* 14, 2035–2053.

Hartmann, D. L., and F. Lo, 1998: Wave-driven zonal flow vacillation in the Southern Hemisphere. *J. Atmos. Sci.,* 55, 1303–1315.

Held, I., and M. J. Suarez, 1994: A proposal for the intercomparison of the dynamical cores of atmospheric general circulation models. *Bull. Amer. Meteor. Soc.,* 75, 1825–1830.

Holton, J. R., 1992: *An Introduction to Dynamic Meteorology*. 3rd ed. Academic Press, 511 pp.

Hoskins, B., and D. Karoly, 1981: The steady linear response of a spherical atmosphere to thermal and orographic forcing. *J. Atmos. Sci.,* 38, 1179–1196.

Inatsu, M., H. Mukougawa, and S.-P. Xie, 2003: Atmospheric response to zonal variations in midlatitude SST: Transient and stationary eddies and their feedback. *J. Climate,* 16, 3314–3329.

Kidson, J., 1988: Indices of the Southern Hemisphere zonal wind. *J. Climate,* 1, 183–194.

Kravtsov, S., J. E. Ten Hoeve, S. B. Feldstein, S. Lee, and S.-W. Son, 2009: The relationship between statistically linear and nonlinear feedbacks and zonal-mean flow variability in an idealized climate model. *J. Atmos. Sci.,* 66, 353–372.

Kushnir, Y., and N.-C. Lau, 1992: The general circulation model response to a North Pacific SST anomaly: Dependence on time scale and pattern polarity. *J. Climate,* 5, 271–283.

——, W. A. Robinson, I. Bladé, N. M. J. Hall, S. Peng, and R. Sutton, 2002: Atmospheric GCM response to extratropical SST anomalies: Synthesis and evaluation. *J. Climate,* 15, 2233–2256.

Li, S., J. Perlwitz, M. P. Hoerling, and X. Chen, 2010: Opposite annular responses of the Northern and Southern Hemispheres to Indian Ocean warming. *J. Climate,* 23, 3720–3738.

Marshall, J., and F. Molteni, 1993: Toward a dynamical understanding of planetary-scale flow regimes. *J. Atmos. Sci.,* 50, 1792–1818.

Maze, G., 2006: Ocean-atmosphere low-frequency interactions in the Southern Ocean. Ph.D. thesis, Université Paris VI, 130 pp. [Available online at http://www.guillaumemaze.org/research/phd.]

——, F. D'Andrea, and A. Colin de Verdière, 2006: Low-frequency variability in the Southern Ocean region in a simplified coupled model. *J. Geophys. Res.,* 111, C05010, doi:10.1029/2005JC003181.

Minobe, S., A. Kuwano-Yoshida, N. Komori, S.-P. Xie, and R. J. Small, 2008: Influence of the Gulf Stream on the troposphere. *Nature,* 452, 206–209.

Peng, S., and J. S. Whitaker, 1999: Mechanisms determining the atmospheric response to midlatitude SST anomalies. *J. Climate,* 12, 1393–1408.

——, and W. A. Robinson, 2001: Relationships between atmospheric internal variability and the responses to an extratropical SST anomaly. *J. Climate,* 14, 2943–2959.

——, W. Robinson, and S. Li, 2003: Mechanisms for the NAO responses to the North Atlantic SST tripole. *J. Climate,* 16, 1987–2004.

Perlwitz, J., S. Pawson, R. L. Fogt, J. E. Nielsen, and W. D. Neff, 2008: Impact of stratospheric ozone hole recovery on Antarctic climate. *Geophys. Res. Lett.,* 35, L08714, doi:10.1029/2008GL033317.

Reynolds, R., and T. Smith, 1994: Improved global sea surface temperature analyses using optimum interpolation. *J. Climate,* 7, 929–948.

Ring, M. J., and R. A. Plumb, 2007: Forced annular mode patterns in a simple atmospheric general circulation model. *J. Atmos. Sci.,* 64, 3611–3626.

Roads, J. O., 1987: Predictability in the extended range. *J. Atmos. Sci.,* 44, 3495–3527.

Rodwell, M., and C. Folland, 2002: Atlantic air-sea interaction and seasonal predictability. *Quart. J. Roy. Meteor. Soc.,* 128, 1413–1443.

Simmonds, I., 2003: Modes of atmospheric variability over the Southern Ocean. *J. Geophys. Res.,* 108, 8078, doi:10.1029/2000JC000542.

Smagorinsky, J., 1953: The dynamical influence of large-scale heat sources and sinks on the quasi-stationary mean motions of the atmosphere. *Quart. J. Roy. Meteor. Soc.,* 79, 342–366.

Son, S.-W., and S. Lee, 2005: The response of westerly jets to thermal driving in a primitive equation model. *J. Atmos. Sci.,* 62, 3741–3757.

Thompson, D. W. J., and J. M. Wallace, 1998: The Arctic Oscillation signature in the wintertime geopotential height and temperature fields. *Geophys. Res. Lett.,* 25, 1297–1300.

——, and ——, 2000: Annular modes in the extratropical circulation. Part I: Month-to-month variability. *J. Climate,* 13, 1000–1016.

——, and S. Solomon, 2002: Interpretation of recent Southern Hemisphere climate change. *Science,* 296, 895–899.

Ting, M., and S. Peng, 1995: Dynamics of the early and middle winter atmospheric responses to the northwest Atlantic SST anomalies. *J. Climate,* 8, 2239–2254.

Verdy, A., J. Marshall, and A. Czaja, 2006: Sea surface temperature variability along the path of the Antarctic Circumpolar Current. *J. Phys. Oceanogr.,* 36, 1317–1331.

Watterson, I. G., 2000: Southern midlatitude zonal wind vacillation and its interaction with the ocean in GCM simulations. *J. Climate,* 13, 562–578.

——, 2001: Zonal wind vacillation and its interaction with the ocean: Implications for interannual variability and predictability. *J. Geophys. Res.,* 106 (D20), 23 965–23 975.

——, 2002: Wave–mean flow feedback and the persistence of simulated zonal flow vacillation. *J. Atmos. Sci.,* 59, 1274–1288.

——, 2007: Southern "annular modes" simulated by a climate model—Patterns, mechanisms, and uses. *J. Atmos. Sci.,* 64, 3113–3131.

——, 2010: Relationships between southeastern Australian rainfall and sea surface temperatures examined using a climate model. *J. Geophys. Res.,* 115, D10108, doi:10.1029/2009JD012120.

White, W. B., 2004: Comments on "Synchronous variability in the Southern Hemisphere atmosphere, sea ice, and ocean resulting from the annual mode." *J. Climate,* 17, 2249–2254.